

SMART-X, “Square Meter, Arcsecond Resolution X-ray Telescope”

A. Vikhlinin^a, P. Reid^a, H. Tananbaum^a, D. A. Schwartz^a, W. R. Forman^a, C. Jones^a, J. Bookbinder^a, V. Cotroneo^a, S. Trolrier-McKinstry^b, D. Burrows^b, M. W. Bautz^c, R. Heilmann^c, J. Davis^c, S. R. Bandler^d, M. C. Weisskopf^e, S. S. Murray^f

^aSmithsonian Astrophysical Observatory, 60 Garden St., Cambridge, MA 02138

^bPennsylvania State University, University Park, PA 16802

^cMassachusetts Institute of Technology, 77 Massachusetts Ave, Cambridge, MA 02139

^dGoddard Space Flight Center, Greenbelt, MD 20771

^eMarshall Space Flight Center, Huntsville, AL 35811

^fJohn Hopkins University, 3400 North Charles Street Baltimore, MD 21211

ABSTRACT

SMART-X is a mission concept for a 2.3 m² effective area, 0.5'' angular resolution X-ray telescope, with 5' FOV, 1'' pixel size microcalorimeter, 22' FOV imager, and high-throughput gratings.

1. OVERVIEW

We describe the Square Meter Arcsecond Resolution X-ray Telescope — SMART-X. This concept leverages an emerging adjustable optics technology to build a mission more scientifically ambitious than the International X-ray Observatory, but more efficiently. Our SMART-X concept includes substantial simplifications and cost reductions relative to IXO — shorter focal length eliminating the extendable optical bench and reducing mass and structural complexity, fewer science instruments, and streamlined operations — and in this, it is similar to many modifications to the IXO studied in the last two years. Adding subarcsecond resolution, SMART-X will build upon *Chandra*'s success and IXO's ambitions, becoming a major and indisputable scientific advance at an affordable cost. To generate sustained support, a mission concept should be able to capture the imagination of the scientific community, and SMART-X will do exactly that.

SMART-X will be capable of addressing almost all of the IXO science goals — growth of SMBH and strong gravity effects; evolution of large scale structure and detection of the WHIM; AGN feedback and cycles of matter and energy. In many areas, SMART-X transcends the scope of IXO. It will be able to carry out surveys to the *Chandra* deep fields depth over 10 deg²; study galaxy assembly processes to $z = 2.5$; and track the evolution of group-sized objects, including those hosting the first quasars, to $z = 6$; open new opportunities in the time domain and high-resolution spectroscopy.

Over the past few years we have developed the concept of the adjustable-optic telescope. With some initial technical suc-

cess, we now believe that it is timely to introduce this approach to the discussion of future directions in X-ray astronomy. The challenge is to develop the optics to a high level of technical readiness over the next several years to provide *Chandra*-like 0.5'' half-power diameter angular resolution with IXO-like area (2.3 m² at 1 keV or ≈ 30 times *Chandra*). This is a tremendous increase — recall that a factor of 4 increase in area from Palomar to Keck was considered a breakthrough at the time. With Keck, there were additional scientific gains from detector advances. For SMART-X, we also plan for advanced instruments: 1) an active pixel sensing imager for surveys, sub-arcsecond imaging, and soft-band response; 2) a 5' \times 5' field of view microcalorimeter with 1'' pixels and 5 eV energy resolution; and 3) a high throughput X-ray grating spectrometer.

The baseline plan for SMART-X optics uses slumped glass mirror segments with deposited piezoelectric actuators energized to correct mirror figure errors from 10'' (achieved for IXO) to $\lesssim 0.5''$. This concept builds upon the mirror development for IXO, both in terms of the thermally formed substrates, as well as mirror alignment and mounting. Work on the optics technology is already underway, with both the baseline option and several alternatives being actively studied.

With funding for mission studies and technology in a few key areas during the current decade, SMART-X can be developed and launched in the 2020's. Whether or not ATHENA or AXISO proceeds in this decade, SMART-X is a qualitative leap forward and is the logical candidate for the major X-ray mission of the 2020's.

2. SMART-X OPTICS

The SMART-X mirror design draws from previous IXO studies and uses slumped glass segments. The 3 m diameter aper-

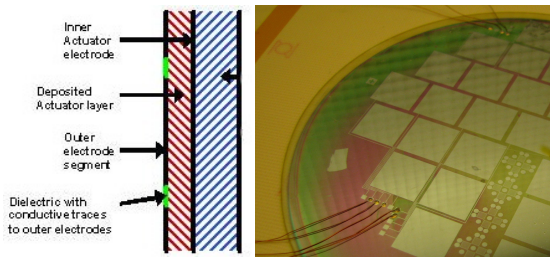


Figure 1. *Left*: Cross-sectional schematic of the PZT cell structure. *Right*: A photo of a flat Corning Eagle™ test mirror with deposited PZT film and a pattern of the independently addressable electrodes.

ture is covered with 292 shells forming a Wolter-type* mirror with a 10m focal length. Mirror segments are 200mm long with azimuthal spans ranging from 150 to 380mm. This model has been ray-traced assuming an Ir coating and accounting for structural obscurations, large angle scattering, contamination, and small alignment errors. Raytrace calculation gives an effective area of 2.3 m^2 at 1 keV (see Fig. 3 below) and shows that the blur due to off-axis aberrations from the Wolter-I design is within $0.5''$ half power diameter out to $2.5'$ off-axis. Losses in effective area due to shadowing and vignetting are less than 50% for all energies out to $\sim 8.5'$ off-axis. At 2 keV, loss of EA is $< 20\%$ within the inner $10'$, providing a useful field of view of at least $20' \times 20'$ for survey work and imaging of extended sources.

The mirror segments are made of either $400 \mu\text{m}$ thick thermally formed glass sheets (similar to those used in LCD displays), or $100\text{--}200 \mu\text{m}$ thick electroformed nickel/cobalt replicated mirror segments. The flight mirror assembly mass is estimated at 890 kg, where the mirror segments and support structure each contribute 50%.

Our approach to achieving $0.5''$ angular resolution with segmented, lightweight mirrors is to make each individual segment adjustable. A ground electrode is deposited on the back of the mirror, then a thin ($1\text{--}5 \mu\text{m}$) layer of piezoelectric material (lead zirconate titanate, or PZT) is deposited on the ground electrode; and lastly, a “pixelated” array of independently addressable electrodes is deposited on the piezo material to form an array of piezo “cells”. As a voltage is applied between the ground electrode and one of the back surface electrodes, strain in the piezo cell causes controllable local bending in the mirror. By controlling the voltage applied to each cell, the correction can be made to match the local figure errors in the mirror, correcting the thin mirror figure to a level not achievable by ordinary means. The appropriate voltage is applied to each cell for the duration of the mission. Nominal leakage current is only $\sim 0.01 \text{ mA}$ at 10 V, so operating power

*Our present estimated are based on ray-trace modeling of a Wolter-1 telescope; we will also consider a Wolter-Schwarzschild and polynomial designs to improve the off-axis point response function.

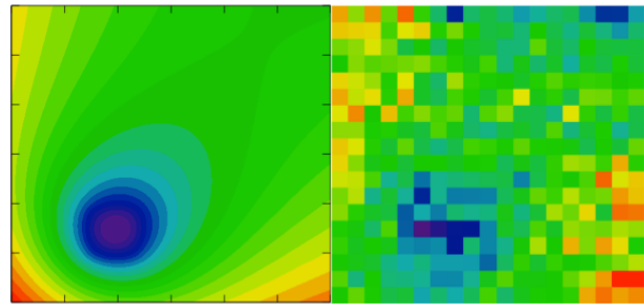


Figure 2. Finite element modeling prediction (*left*) and deformation (*right*) in response to an individual cell activation in one of the first experiments. The substrate response to energizing multiple cells is now measured with much greater accuracy (Ried et al., these proceedings.)

even for 10^6 adjusters is a few hundred watts.

We project that a mirror figure quality corresponding to $0.5''$ angular resolution can be achieved by having the individual segments adjusted essentially once. Figure errors after mounting and alignment will be measured by optical surface metrology. These errors as well as deformations due to gravity release and the nominal on-orbit thermal environment will be corrected by applying an optimal set of voltages to each mirror segment. Depending on mission safety requirements, the piezos can either be left energized through launch, or the power supplies turned off, and the piezos energized once on-orbit.

SAO and PSU working together have made significant progress with adjustable X-ray optics, and we consider the technology to be at TRL2 and approaching 3†. Thin films of piezoelectric material was successfully deposited on flat test mirrors (Fig. 1), and the energizing of that piezo to produce a localized figure change consistent with expectations (Fig. 2). Piezo thickness, properties, and achieved strain (800 ppm) meet requirements dictated by starting with an $\sim 10''$ PSF for an uncorrected mirror pair and correcting it to $< 0.5''$.

Investigations of mirror lifetime, stability, and repeatability have begun. We note that PZT has been used in space for focus control on the AIA telescopes on the Solar Dynamics Observatory,² and also used in the Fine Guidance Sensors developed for JWST.³ The thermal sensitivity of thin film PZT is very small, $\sim 1\%$ per degree C at nominal SMART-X mirror and laboratory temperatures, $20\text{--}21^\circ\text{C}$.⁴ Lifetime applied voltage cycling tests confirm that a required level of stability of the piezoelectric coefficient can be achieved over space mission lifetimes.^{5,6}

We are developing a finite element analysis model for adjustable mirror segments to study strategies for correcting

†Note also that a subset of this technology is already being used for 1-D correction of synchrotron X-ray optics.¹

“generic” figure errors and develop optimization techniques. To date, we have demonstrated that distortions in one of the slumped glass segments produced for IXO development and installed on a flight-like mount can be decreased by a factor of > 15 , improving the angular resolution from $10''$ to $0.6''$ HPD (Reid et al., these proceedings). We also studied the gravity release errors and found that they are small, $\sim 0.11''$ rms, and can be almost entirely removed by piezo actuators (to $\sim 0.01''$ rms,⁷).

For more information on the current state and development plans for the adjustable X-ray optics technology, see the paper by P. Reid et al. in this proceedings. Here we note, that the technology can be brought to a NASA “readiness level 6” by 2019. We are also on track to achieve within the next 3 years an adjustable mirror pair whose performance, consistent with subarcsec imaging, will be verified in an X-ray test.

3. SMART-X SCIENCE INSTRUMENTS

We envision three science instruments for SMART-X. The deployable Critical Angle Transmission Grating Spectrometer (CATGS) will provide a resolving power of $R > 4000$ with large collecting area across the 0.2–1.2 keV energy band. The two prime focus imaging instruments, on a movable translation stage, are complementary and provide some redundancy. The Active Pixel Sensor Imager (APSI) is optimized for high-resolution imaging, provides a large FOV ($22' \times 22'$) for surveys, and has excellent response at $E < 0.5$ keV for studies of high-redshift objects. The X-ray Microcalorimeter Imaging Spectrometer (XMIS) provides 5 eV spectroscopy and good high- E efficiency, while still maintaining $1''$ imaging. The zeroth-order image in the prime focus can be taken using either APSI or XMIS.

3.1 Critical Angle Transmission Grating Spectrometer

The X-ray Grating Spectrometer (CATGS) provides high-resolution, very high-throughput spectroscopy in the 0.2–1.2 keV band. The CATGS consists of an array of Critical Angle Transmission (CAT) gratings on a deployable mount located behind the flight mirror assembly, together with a dedicated readout subsystem on the SMART-X focal plane. The instrument architecture is similar to that of *Chandra*’s HETG, which was built by the CATGS team and which has been operating successfully for more than 12 years.

The CAT grating is a novel optical element⁸ that combines the low mass and relaxed alignment and figure tolerances of a transmission grating with the excellent diffraction efficiency and resolving power of blazed reflection gratings used in high-diffraction order. CAT gratings are manufactured at MIT from silicon wafers using micro-fabrication techniques. The technical readiness of CAT gratings was evaluated during

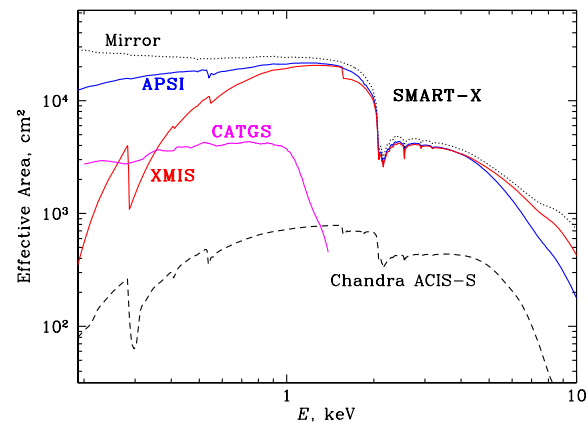


Figure 3. Effective area of the SMART-X optics and science instruments.

IXO definition studies and judged to be at TRL3 in 2009 on the basis of prototype grating performance measurements at a synchrotron radiation facility. A technology development plan was developed then and substantial progress on fabrication of grating support structures has been made in the past two years. We expect to achieve TRL4 in 2012. With adequate funding, we expect to reach TRL5 no later than 2015.

The sub-arcsecond angular resolution of the SMART-X mirror enables excellent dispersive spectral resolution without use of the sub-aperturing required for optics similar to IXO’s. As a result, the CATGS gratings can be deployed over the entire mirror aperture for maximum effective area (for SMART-X, our baseline is to cover 50% of the aperture, constrained by cost), while using a single linear readout array which substantially reduces the complexity and cost of the instrument. Thus, SMART-X/CATGS exploits technologies developed for IXO to provide extraordinary improvements in spectral resolving power and effective area. With a 3.0° blaze angle optimizing the tradeoff between efficiency and the high-energy cutoff, CATGS will achieve a **resolving power** of $R > 4000$ across the 0.2–1.2 keV band and a 0.4 m^2 **collecting area**.

The CATGS readout subsystem, CATGSR, is a linear array of Si-based active pixel sensors (§3.2 below), placed on a fixed platform ~ 60 cm off the primary focus on a separate focusing mechanism and aligned tangent to the Rowland torus. The energy resolution of the CATGS readout provides spectral order sorting. The 0-th order image can be provided by either the APSI or the XMIS arrays. Because the silicon CAT gratings are relatively thin ($6 \mu\text{m}$), the prime imaging focus retains significant effective area at $E > 1$ keV even with the gratings in the beam.

Table 1. *SMART-X* Science Instrument Capabilities

	Energy Band	Energy Resolution	Angular Resolution	Field of View
CATGS	0.2–1.2 keV	$E/\Delta E > 4000$	0.5'' across dispersion	...
APSI	0.2–8 keV	37 eV @ 0.3 keV, 120 eV @ 6 keV	0.5'' mirror, 0.33'' pixels	22' × 22'
XMIS	0.2–10 keV	5 eV	1'' pixels	5' × 5'
Mirror	0.1–10 keV	...	0.5'' on-axis, 0.7'' @ 2.5', 4'' @ 10'	10' radius

3.2 Active Pixel Sensor Imager.

The *SMART-X* Active Pixel Sensor Imager (APSI) is an array of active pixel sensors tuned for high-resolution, wide-field imaging at the prime focus, and providing excellent soft-band sensitivity needed for observations of high-redshift sources. The same technology will be used for a separate array, CATGSR, needed for the readout of the dispersed CATGS spectra.

Si-based sensors based on CMOS technology already meet many of the *SMART-X* requirements. CMOS detectors have been developed along two primary lines: CMOS hybrids (e.g., the PSU/Teledyne⁹ and the MIT three dimensional integrated circuit technology¹⁰), and monolithic CMOS (e.g., SAO/Sarnoff¹¹ and the MPI DEPFET¹²). Hybrid CMOS devices have deep depletion for good QE at high- E , they are four side abutable for constructing large mosaics, but currently show high read noise, $\sim 10\text{ e}^-$ and poor low energy resolution. Monolithic devices demonstrate low readnoise, $< 2\text{ e}^-$, good low-energy response, but currently have small depletion depth, $< 20\text{ }\mu\text{m}$, limiting QE above 2 keV.

Straightforward, achievable developments will ensure that all requirements, listed below, are met and TRL5 reached by 2020. We aim for a **pixel size** of $16\text{ }\mu\text{m} = 0.33''$, smaller than the angular/dispersive resolution of the mirror. APSI is a > 16 megapixel array covering at least $22' \times 22'$ FOV in the prime focus. We will work to reduce the pixel size to better oversample the PSF and increase the number of pixels to maintain a $\sim 20'$ FOV. CATGSR is a linear array with a total length of $\sim 20\text{ cm}$. Full-frame **readout rates** for both arrays are 100 s^{-1} to minimize dark current and optical load. A thin, 10–20 nm, layer of Al (achieved at PSU) capped with an Al_2O_3 layer of comparable thickness (under development at MIT) serves to block stray light from XUV to the near IR with minimal impact on soft X-ray response, resulting in high QE for the sensor+filter system down to $E \lesssim 0.2\text{ keV}$. Very optically bright sources can be observed with XMIS which has a thick filter. **Energy resolution** in both cameras is Fano-limited over the entire band. APSI will have high-speed **windowing capability** to avoid pileup and perform μs timing of bright sources. Devices will have sufficient radiation hardness to withstand the projected mission lifetime without significant degradation.

We note that there are important distinctions in the requirements for the APSI and CATGSR cameras. CATGSR does not

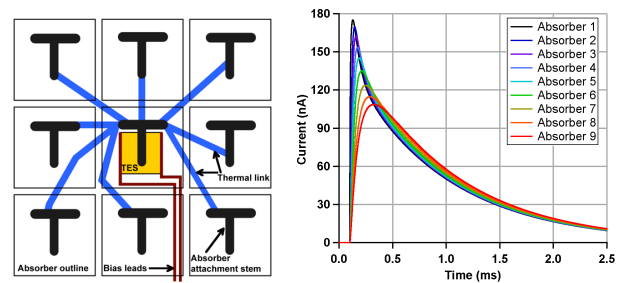


Figure 4. *Left*: Schematic diagram of the Hydra concept, showing nine absorbers, each with a different thermal conductance, connected to a single TES. Each absorber is supported above the TES and solid substrate using small stem contact regions (shown as “T” shapes here). *Right*: Simulated 9-pixel Hydra noise-less pulse shapes for a photon energy of 100 eV. Absorber 1 is the most strongly coupled absorber to the TES.

require sensitivity above $\sim 2\text{ keV}$, but it needs high quantum efficiency and energy resolution down to the lowest possible energy (100 eV). The monolithic technology is a good match for both of these aspects of performance. For the APSI, the higher energy response is more required, while a higher readout noise can be tolerated. These aspects better match the performance of the hybrid detectors and the general direction of their technology developments. Therefore, while the goal is identical technology for both APSI and CATGSR, we note that the two cameras can at the very least be built using separate, monolithic and hybrid, sensors. The sensors are sufficiently similar so that nearly identical electronics packages can be used to drive and process the data.

3.3 X-ray Microcalorimeter Imaging Spectrometer.

Microcalorimetry is a powerful technology for high-resolution X-ray spectroscopy that has been used in numerous experiments and has progressed steadily, with $\Delta E < 2\text{ eV}$ achieved in recent laboratory tests. However, it has been a challenge to use this technology in arrays with good imaging capabilities. This is now changing. For *SMART-X*, we baseline the X-ray Microcalorimeter Imaging Spectrometer (XMIS) to provide high spectral resolution over a 0.2–10 keV band, as well as high angular resolution over a moderate field of view.

XMIS is a 300×300 array of $50\text{ }\mu\text{m}$ pitch pixels, uniformly covering a $5' \times 5'$ **field of view** with $1''$ **spatial resolution**.

While 90,000 appears to be a large number of pixels for microcalorimeters, the instrument we envision will be similar in cost and resources to that proposed for AXSIO. This assertion is based on current status and advances expected from existing and funded development programs over the next several years.

One cornerstone of our design is the use of position-sensitive microcalorimeters known as “Hydras”, where a single Transition Edge Sensor (TES) is coupled to more than one discrete absorber (see Fig. 4 for a 3×3 Hydra). Each absorber element has a different thermal conductance to the sensor that results in position information being encoded in the pulse shape (Fig. 4b). This type of device has been successfully fabricated and tested in larger sizes for astrophysics and performs as predicted.^{13,14} Algorithms have been developed to identify X-ray events down to low energies, ~ 0.2 keV. Hydras with 16 absorbers per TES have been designed and are being tested, and Hydras with as many as 25 absorbers are considered possible. We estimate that < 5 eV **energy resolution** (FWHM, rms average within one Hydra) will be possible with 5×5 arrays of individual 50 μm absorbers. The maximum number of wire pairs between any two TESs is 15–19, which we estimate can be accommodated between absorbers in a planar geometry using the $\sim 4 \mu\text{m}$ wire pitch stripline wiring already demonstrated in arrays designed for solar applications.

The estimated **count rate capability** is 20 cnt s^{-1} per TES for the 25-absorber Hydra. The resulting throughput is 0.8 cnt s^{-1} per $1''$ pixel, sufficient to image all but the brightest known extended X-ray sources. For example, the brightest spots in Cas-A will still be under the saturation threshold. In the M87 field (Fig. 6d), only the AGN and the brightest knot in the jet will be saturated.

The current TRL of the XMIS subsystems (detector, read-out, focal-plane assembly, and the cryogenics) with respect to the SMART-X requirements range from 2–3 to 5, and ongoing technology development efforts will raise them to TRL5 for all these components by 2015–2017. For example, the use of current-steering multiplexing¹⁵ has a 3-year program of ROSES-APRA technology development funding. With the speed necessary for the SMART-X TES design, we conservatively predict that the ability to multiplex 64–128 TESs per read-out channel will be demonstrated within three years. Combined with the use of 25 absorber Hydras, the number of required readout channels will be similar to that needed for the AXSIO XMS design (~ 68).

4. SMART-X SCIENCE

4.1 Core IXO science.

Except for sensitivity at $E > 10$ keV and timing for 10^6 cnt s^{-1} , SMART-X meets or exceeds all requirements for achieving the core science goals of the IXO.

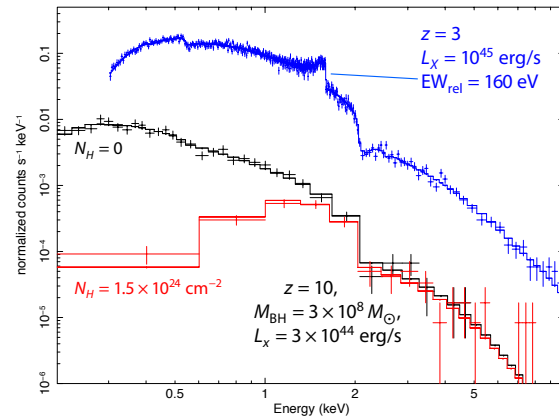


Figure 5. 300 ksec SMART-X/APSII observation of a Sloan $z = 6$ quasar progenitor at $z = 10$. Growth at 10% Eddington rate has been assumed, resulting in $M_{\text{BH}} = 3 \times 10^8 M_{\odot}$ and unobscured $L_X = 3 \times 10^{44} \text{ erg s}^{-1}$ (2–10 keV). Such quasars are easily detectable even if highly obscured (red). Blue: 300 ksec XMIS observation of a “typical” eRosita AGN at $z = 3$ with a relativistically broadened Fe line ($\text{EW} = 160 \text{ eV}$).

What happens close to a black hole? Although the effective area at 6 keV is 0.17 m^2 , a factor of 4 below IXO, SMART-X still will be able to measure motions of individual hot spots and test GR in 5–10 X-ray bright SMBHs through time-resolved Fe line spectroscopy.

When and how did SMBHs grow? Similarly, BH growth history can be constrained¹⁶ through observations of the BH spin distribution in a sample of ~ 40 low- z SMBH (vs. 300 for IXO). For a handful of objects, the measurements can be done at z up to 3 (Fig. 5). Additional insights into the growth of SMBHs will be provided through studies of their first generations ($z > 6$) through surveys, for which SMART-X capabilities are unique (§4.5).

How does large scale structure evolve? The SMART-X sensitivity for weak absorption lines in the WHIM exceeds that of IXO by a factor of > 2 because of a higher throughput and resolving power [$\propto (AR)^{1/2}$]. SMART-X exceeds all requirements for measuring the growth of cosmic structure and evolution of the elements through observations of galaxy clusters to $z \sim 2$. A “precision cosmology” program¹⁸ resulting in accurate structure growth measurements to $z \sim 1.5$ can be executed in < 10 Msec in combination with the weak lensing data from Euclid.

What is the connection between supermassive black hole formation and evolution of large scale structure? **Cosmic feedback.** We estimate that the baselined 5 eV energy resolution of XMIS will be sufficient for plasma line diagnostics and velocity structure measurements in the intracluster and interstellar media. With arcsecond angular resolution, detections of AGN feedback in clusters can be extended to $z \sim 1$,

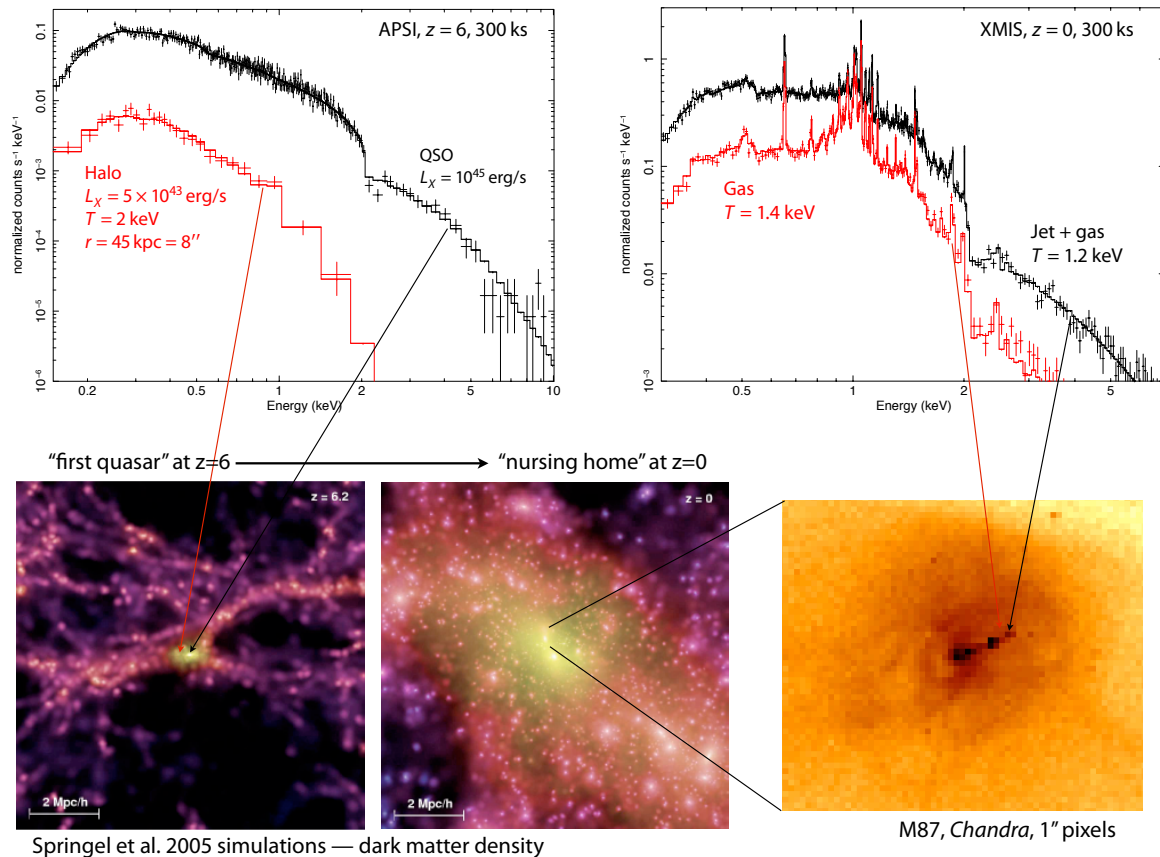


Figure 6. *SMART-X* view of the environment of the “first quasars” and their descendants at $z = 0$. Sloan quasars must be located in the most massive halos existing at $z = 6$, $M = (2 - 6) \times 10^{12} M_{\odot}$ with $r_{\text{vir}} \approx 50 \text{ kpc}$.¹⁷ These halos resemble cores of today’s rich galaxy clusters both in terms of the dark matter density and X-ray properties [$T = 1.5 - 3 \text{ keV}$, $L_X = (2 - 9) \times 10^{43} \text{ erg s}^{-1}$]. *SMART-X* will be able to separate this faint halo from the bright quasar emission *spatially* in a 300 ksec APSI observation. Descendants of the first quasars at $z = 0$ are at the centers of rich galaxy clusters. A 300 ksec observation of a low- z cluster core with XMIS yields enough counts for detailed spectroscopy in $1'' \times 1''$ regions.

spatially-resolved velocity structure measurements can be done at $z \sim 0.5$. True $1''$ spectro-imaging will illuminate the physics of AGN interactions with the cooling gas in the cluster cores through detailed measurements of the turbulence power spectrum and observations of flows near the hot/cold gas interfaces (Fig. 6b).

How does matter behave at very high density? CATGS throughput exceeds the IXO performance by a factor of 4, correspondingly improving efficiency of the neutron star equation of state measurements.

SMART-X capabilities make it a versatile observatory with strong appeal to a very broad cross-section of the astronomical community. All areas of active X-ray astronomical research today — evolution of galaxy clusters and hierarchical structure growth; metal enrichment of the IGM reflecting the history of star formation; AGN feedback, duty cycles and relation between the radio- and quasar modes; source populations in

nearby galaxies; physics of supernova remnants; etc. etc. — will reach new heights with *SMART-X*.

The high angular resolution emphasized in the *SMART-X* design enables science well beyond that considered by Astro2010 for IXO. It will open new windows for X-ray astronomy in studies of the high- z Universe, in the time domain, and in high-resolution spectroscopy. In the space remaining, we give only a few examples of what *SMART-X* would achieve for studies of galaxy formation and growth of supermassive black holes.

4.2 Supermassive black holes and their environment to $z = 6$ and beyond.

Studies of the first generation of black holes and their host galaxies which by $z \approx 6$ have ionized nearly all of the hydrogen in the Universe is one of the major topics highlighted by Astro2010.

Quasars at $z \sim 6$, discovered in the SDSS and other surveys,^{19–21} are extremely luminous and massive, $M_{\text{BH}} \sim 10^9 M_{\odot}$.²⁰ To form such a massive BH at high z is a great challenge for theory. Depending on the typical accretion rate, the progenitor masses at $z = 10$ range from $M_{\text{BH}} \sim 3 \times 10^8 M_{\odot}$ for $\dot{M} = 0.1 \dot{M}_{\text{Edd}}$ to $\sim 7500 M_{\odot}$ for an Eddington rate. Observations of this progenitor population are one of the best ways to solve the puzzle of the seed BH origin.²²

Many $z = 6$ quasars are detected in short *Chandra* observations to have $L_X \sim 10^{45} \text{ erg s}^{-1}$.²³ Assuming that $L_X \propto M_{\text{BH}}$, we expect $L_X \approx 3 \times 10^{44} \text{ erg s}^{-1}$ for a $3 \times 10^8 M_{\odot}$ SMBH at $z = 10$. SMART-X sensitivity is sufficient (Fig. 5) for spectroscopy of such quasars, even if they are highly obscured and thus undetectable in the optical or IR. In a medium-sensitivity survey observation, 100 ksec with APSI, a 10 photons detection threshold at $z = 10$ corresponds to a low-luminosity AGN, $L_X = 6.5 \times 10^{42} \text{ erg s}^{-1}$ or $M_{\text{BH}} \approx 6.5 \times 10^6 M_{\odot}$. SMART-X will be able to survey $\sim 10 \text{ deg}^2$ to this depth, so any significant population of such SMBH at $z = 10$ will be uncovered.

The growth of SMBH is intimately connected with the properties and environment of their host galaxies. SMART-X will be able to directly study the connection to $z = 6$. Springel et al.¹⁷ argue that the $M_{\text{BH}} \sim 10^9 M_{\odot}$ Sloan quasars must be located in the biggest galaxies and hence in the biggest dark matter halos existing at that epoch. These host halos resemble the cores of today's galaxy clusters both in their X-ray properties and dark matter density, $M_{\text{tot}} = (2 - 6) \times 10^{12} h^{-1} M_{\odot}$, $r_{\text{vir}} \approx 50 \text{ kpc}$, $T = 1.5 - 3 \text{ keV}$ and $L_X = (2 - 9) \times 10^{43} \text{ erg s}^{-1}$. Although the halo X-ray emission is only a small fraction of the quasar's flux, and normally is undetectable, SMART-X, can easily separate the quasar and the halo *spatially* ($1'' = 5.5 \text{ kpc}$ at $z = 6$), and in a 300 ksec APSI observation the halo's gas temperature will be measured (Fig. 6).

Through detailed SMART-X spectroscopy of quasars at $z \leq 6$, we can detect powerful SMBH-driven winds,²⁶ use Fe line to detect the presence of multiple SMBHs,²⁷ and in some cases observe strong gravity effects (Fig. 5).

Fast-forwarding to $z = 0$, the SMBHs of the first quasars should lie at the centers of rich galaxy clusters,¹⁷ and many have switched to "radio-mode" (e.g.,²⁸). A moderately-deep XMIS observation (300 ksec) of a low- z cluster will provide an amazingly detailed picture of the "nursing home of the first quasar"; enough photons for detailed spectroscopy will be collected in individual $1'' \times 1''$ pixels (Fig. 6, right). Even at $z = 0.5$, SMART-X will be able to observe interactions of AGNs with the cluster gas with a remarkable level of detail.

4.3 Galaxy and star formation.

Galaxy formation is also highlighted in the Astro2010 report. Evolution of star formation in objects of different mass is now tracked to $z \lesssim 1$ in surveys such as COSMOS.²⁹ The results are

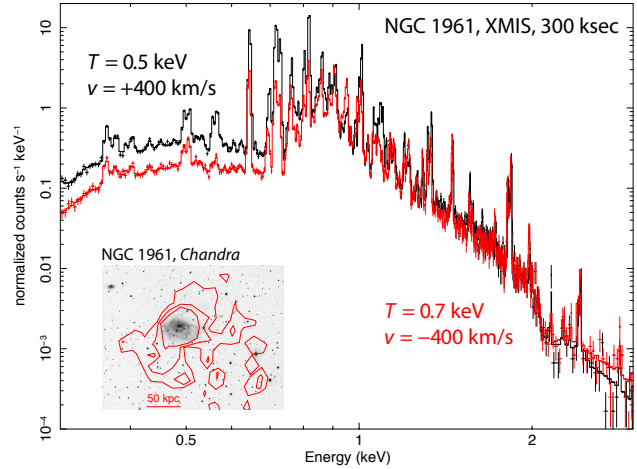


Figure 7. Simulated 300 ksec SMART-X/XMIS observation of the hot gaseous corona around NGC 1961.²⁴ The best-fit *Chandra* model was separated into two components with slightly different temperatures and bulk velocities expected in massive halos.²⁵ Temperatures, ionization states, and chemical abundances of different elements are easily derived from such spectra, and relative velocities can be measured to $\pm 30 \text{ km s}^{-1}$.

puzzling in that $> 70\%$ of baryons in galaxy-sized halos are missing (e.g.,³⁰). Almost certainly, these baryons are expelled from the galaxy halos. Possible ejection mechanisms are energy feedback from the SMBH growth,³¹ galactic winds driven by stellar feedback,³² or self shock-heating of the infalling gas inside the halos with $M_{\text{tot}} > 3 \times 10^{11} M_{\odot}$.²⁵ Regardless of the exact mechanism, for the gas to leave a halo, a significant fraction of it must be heated to \sim the halo virial temperature, $T \gtrsim 0.3 \text{ keV}$ for large galaxies, making it observable only in the X-rays.

Stellar material in the galaxies is observed in the optical near-IR; molecular gas and dust deep inside the star-forming regions will be detected by ALMA and EVLA; cold hydrogen in the 100-kpc galaxy halos at high redshifts is observed in Ly- α .³³ The picture is incomplete without observations of the hot gas phase expected to contribute $\sim 1/3$ of the total baryonic mass. Thus X-ray data are essential to complete the observational picture of galaxy assembly. As we discuss below, the hot gas should be detectable with SMART-X around massive star-forming galaxies in a wide range of redshifts reaching to $z = 2.5$.

To estimate the detectability of hot gas halos at high redshifts with SMART-X, we consider kinematic studies of Ly- α selected galaxies at $z \approx 2.5$.³⁸ These are active, star-forming galaxies ($\text{SFR} \approx 30 M_{\odot} \text{ yr}^{-1}$), whose halos ($M_{\text{tot}} \sim 9 \times 10^{11} M_{\odot}$) contain on average $7 \times 10^{10} M_{\odot}$ of cold gas with bulk velocities $500 - 800 \text{ km s}^{-1}$. Collisions of individual gas clouds at such velocities should heat a fraction of the halo baryons to $T \sim 1 \text{ keV}$. Assuming that the mass of hot and cold

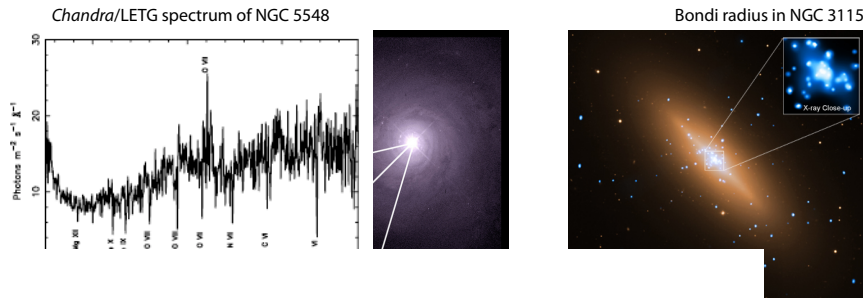


Figure 9. *Left:* *Chandra*/LETG observation of an outflow in the vicinity of the AGN in NGC 5548.³⁶ *Right:* Estimated Bondi radius in NGC 3115 is $4''$ with FWHM of the central emission peak $\approx 3''$.³⁷ *SMART-X*/CATGS energy resolution for such sources will be $R > 1000$, while providing $0.5''$ angular resolution across the dispersion direction.

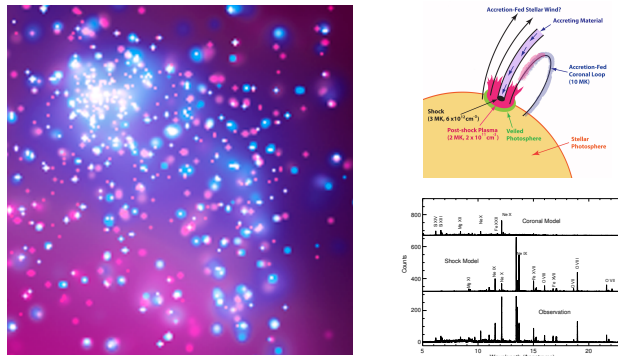


Figure 8. *Left:* *Chandra* 60 ksec observation³⁴ of the Trumpler 14 complex in the Carina Complex ($5' \times 5'$ region) contains ~ 1000 stars down to $\log L_x \approx 29.8 \text{ erg s}^{-1}$. A similar single observation with *SMART-X*/XMIS will result in detection of $\sim 10,000$ stars and provide high-resolution spectra of a dozen OB stars and hundreds of flaring/active T Tauri stars. X-ray spectroscopy is a key diagnostics of the physics of coronae of active stars (*right*, from³⁵).

gas phases within the halo is similar (as in NGC 1961, see below), one expects X-ray luminosities of $3 \times 10^{42} \text{ erg s}^{-1}$ in a diffuse component extending to $\sim 80 \text{ kpc} = 10''$. A 300 ksec observation of such an object with *SMART-X*/APSI will yield 500 photons, enough to measure the temperature, density, and overall morphology of the gas halo. The halo will be easily separated spatially from the X-ray flux of discrete sources within a compact star-forming region of the galaxy.

Less speculative are the prospects for detailed observations of circumgalactic gas around low- z spirals because several detections have already been made with *Chandra*. Examples include well-known observations of galaxy-scale winds in M82, and a recent detection of a 50 kpc-scale diffuse halo in NGC 1961.²⁴ The NGC 1961 halo has an X-ray luminosity of $4 \times 10^{40} \text{ erg s}^{-1}$ and temperature of 0.6 keV, and is estimated to contain $5 \times 10^9 M_\odot$ of hot gas within 50 kpc and $2 \times 10^{11} M_\odot$ within the virial radius, roughly the stellar mass in the system and $4\times$ the mass of the cold gas. Such a halo observed for 300 ksec with *SMART-X*/XMIS would provide a uniquely informative measurement of the thermal, chemical, and kinematic structure of the hot gas (Fig. 7).

To complete the X-ray view of cosmic star formation, *SMART-X* will be able to look deep inside star forming regions in the Milky Way (Fig. 8), and study processes ranging from the physics of protoplanetary disks^{35,40} to elemental abundance, shocks, absorption and charge-exchange emission in the surrounding ISM.

4.4 High-resolution spectroscopy.

The combination of *SMART-X* mirrors with the CAT transmission gratings will provide immensely powerful spectroscopic capabilities in the soft X-ray band. Absorption line observations of the gas outflows around AGNs^{36,41} will be routine, and measurements of the neutron star equation of state⁴² feasible. The new aspect of CATGS is that it is highly dispersive and will provide $R = 1000$ resolving power even for sources with a size of $3'' - 5''$, while the $0.5''$ spatial resolution will be available across the dispersion direction. Therefore, CATGS will be able to make detailed spectro-imaging observations of slightly extended objects such as the emission from within the Bondi radius in NGC 3115 ($r = 4''$, $T \approx 0.5 \text{ keV}$,³⁷ Fig. 9b).

4.5 Surveys.

SMART-X can carry out surveys matching the scope of the future deep optical, IR, and mm/submm surveys. Its instrumental background is close to *Chandra*'s because of the same focal length and similar orbit, $\approx 10^{-6} \text{ cnt arcsec}^{-2} \text{ s}^{-1}$. If we consider detections in the 0.7–2 keV band where the Galactic foreground contamination is low,⁴³ then for typical power law spectra, *SMART-X*/APSI has a factor of ~ 50 higher throughput than *Chandra*/ACIS-I — a combined gain of factors of 30 and 1.6 due to the mirror area and soft-band QE of APSI, respectively. Therefore, the sensitivity limit of the 4 Msec *Chandra* Deep Field South will be reached with *SMART-X* in 80 ksec. Sensitivity will be fully photon-limited because even at $10'$ off-axis where the PSF is $4''$ HPD, there will be only 1 background event per resolution element at this exposure. The *Chandra* PSF degrades to $4''$ HPD at $7'$ off-axis, so *SMART-X* provides not only a higher sensitivity but also a wider FOV. The grasp of *SMART-X* is a factor of 98 higher than *Chandra*'s.

A 10 deg^2 survey to the CDFS depth can be carried out in 8.1 Msec. A 4 Msec individual pointing will reach on-axis sensitivity (for 10 cnt detections) of $3.0 \times 10^{-19} \text{ erg s}^{-1} \text{ cm}^{-2}$ in the 0.5–2 keV band, corresponding to $L_X^{(2-10)} = 3.3 \times 10^{41} \text{ erg s}^{-1}$ at $z = 10$.

4.6 Time-domain X-ray astronomy.

With *SMART-X* operating in the 2020's and potentially beyond, there will be a sufficient time span relative to *Chandra* to observe secular evolution in a number of astronomical objects, thus opening a completely new window for X-ray astronomy. Examples include the evolution of the compact object and shocked plasma in Cas-A and other young supernova remnants ($\Delta t/\text{age} \sim 10\%$) and the spectacular fireworks display in SN1987A expected over the next few decades as increasing amounts of metal-rich ejecta are lit up by the reverse shock. Past activity of the Milky Way's central black hole can be tracked by evolution of its light echos on the molecular clouds around Sgr A*. Repeated 100 ksec observations of a single field \sim twice a year over a 5 years span will provide a detailed picture of variability for 100's of high-redshift AGNs.

5. SMART-X MISSION

We envision the launch of *SMART-X* to a 700,000 km orbit about the L2 point. The total mass of the *SMART-X* payload is 2863 kg (this includes an estimated mass, 1300 kg, of the spacecraft with the optical bench). With a 30% growth contingency and 200 kg propellant, the total "wet" mass is 3922 kg. This is comfortably launchable with Atlas V-541 ($> 5000 \text{ kg}$ throw mass).

The mission design and operations share great similarities to both *Chandra* and AXSIO. Compared to *Chandra*, *SMART-X* has a slightly lower (17%) overall mass, while the telescope assembly mass is 28% less. Key requirements — including alignment, stability, pointing control and aspect determination — will be essentially the same, and therefore require no new technology. The main difference is higher peak science data rates, and increased power requirements for thermal control of the optics and operating XMIS. Compared to AXSIO, *SMART-X* will share the same general layout, but with an updated optic, a second focal plane instrument, and a translation stage, resulting in $\sim 30\%$ larger mass and power requirements. Much of the *Chandra* ground software for all aspects of operations and science can be reused for *SMART-X*.

5.1 Cost.

The major new technology development required to realize the *SMART-X* mission is the adjustable optics to provide the large area, low mass, $0.5''$ resolution telescope at an affordable price. The cost of this program is estimated at \$45M in the next 6–8 yr — a rather modest investment to achieve

the gains possible with *SMART-X*. An additional technology investment of $\sim \$30\text{M}$ is required to bring the science instruments to TRL 5/6.

Even though the *SMART-X* concept is new and has not been evaluated by the MDL, much of the work done for AXSIO is directly relevant, as is the *Chandra* experience. We can start with the detailed assessment done by the AXSIO team and the MDL and then identify differences for *SMART-X*. The summary is given in Table 2 and the cost methodology follows.

5.1.1 Flight Mirror Assembly

Overall, we estimate the total *added cost for the SMART-X mirrors to be at \$170M, including 50% reserves*. It includes doubling the AXSIO cost (\$54M) for mandrels — while essentially the same number of mandrel pairs is required (*SMART-X* has more shells but a single mandrel can be used for up to 3 adjacent shells because the optics are adjustable), the mandrels require better upper-mid frequency figure and the mandrels have larger area. The cost of AXSIO module facilities (\$30M) is scaled by a factor of 2 to account for the greater accuracy required, and then by the number of modules (42 vs. 60 for AXSIO), resulting in a net increase of \$12M. The AXSIO cost of mirror manufacture (\$174M) is increased by 5% or \$8.7M to account for additional metrology time (estimated at 1 hour per mirror) to calibrate the PZT adjuster influence functions for each segment. Note that the total number of mirror segments is similar, 8256 for AXSIO vs. 8016 for *SMART-X*, which essentially eliminates any other impacts for the larger aperture.

These components add \$75M to the cost of production of AXSIO mirrors, \$282M, leading to a total of \$357M for *SMART-X*. Given the novelty of the *SMART-X* mirror technology, we believe it is prudent to allow for 50% reserves, resulting in \$536M, an overall increase of \$170M relative when we include 30% reserves carried by AXSIO.

5.1.2 Science instruments and other differences.

SMART-X introduces an additional science instrument, APSI. The CATGSR array, using identical technology, replaces the CCD-based readout array for AXSIO/XGS (\$35M). Taking into account a streamlined configuration of the CATGS readout, we estimate the cost of APSI +CATGSR as double that of the AXSIO/XGS readout, an additional \$35M.

To achieve 4000 cm^2 gratings effective area, CAT gratings facets need to cover a factor of 5.3 larger aperture area compared to AXSIO/XGS. Scaling the AXSIO/XGS fabrication cost (\$15M) by the area, we estimate an added cost of \$65M for *SMART-X*.

We assume no additional costs for the XMIS. The translation table cost is estimated at \$37M from the *Chandra* cost;

Table 2. Resource and cost comparison of *SMART-X* and AXSIO

	SMART-X		Δ from AXSIO		Cost ¹
	m, kg	P, W	m, kg	P, W	
Mirrors	890	1000	418	650	\$170M
Science instruments & spacecraft systems					\$188M
APSI +CATGSR	107	300	65	250	
XMIS	358	1100	0	0	
Gratings	64	0	52	0	
Translation stage	144	0	144	0	
Integration & Test					\$52M
Atlas V-541 launch					\$20M
Total ²	2863	2817			

¹ All added costs include reserves, as explained in the text. ² Total mass and power also include spacecraft systems.

an extra \$3.7M is required for larger solar panels, and \$4M for upgraded aspect cameras.

The added cost of the science instruments and upgrades to the spacecraft systems is thus \$144.7M, **or \$188M including 30% reserve.**

To account for the extra complexity of X-ray test facilities and testing efforts, we double the AXSIO cost (\$52M, including 30% reserve). Finally, the cost of launch with Atlas V-541 is \$20M higher than that with 521 for AXSIO.

Adding all these extra components to an estimated end-to-end cost of the AXSIO mission, \$1,898M, we obtain a **total end-to-end mission cost of \$2,328M for SMART-X.**

5.1.3 Testing vs. *Chandra* cost.

We can independently cross-check the above cost estimates against the actual cost of building *Chandra*, \$2,521M in FY2012 dollars. This should be compared against the estimated cost of *SMART-X* excluding launch, ground system, and post-launch operations — \$1,838M, obtained by adding *SMART-X* extras to the corresponding cost of AXSIO. The inflated *Chandra* cost is most certainly an overestimate because it is based on labor rates while parts and components have escalated less. Also, technology investments already made as well as the *Chandra* knowledge base and experience are significant savings factors for *SMART-X* (e.g., optics metrology is in hand for *SMART-X* but had to be developed for *Chandra*).

The *SMART-X* mission concept for a 2.3 m², 0.5'' resolution X-ray telescope, with 5' FOV, 1'' pixel size microcalorimeter, 22' FOV imager, and high-throughput gratings, is challenging. However, we will be working with known requirements and capabilities, once the mirror technology is proven. The science will be extraordinary.

REFERENCES

- Alcock, S., 2011, in *4th Workshop on Adaptation and Active X-ray and XUV Optics*, <http://www.diamond.ac.uk/Home/actop/programme.html>
- Shine, R.A. et al., 2010, AGU Fall Meeting
- Rowlands, N. et al., 2004, SPIE Proc., 5487, 646
- Wolf, R. A. & Troiler-McKinstry, S., 2004, J. Appl. Phys., 95, 1397
- Shepard, J. F. Jr. et al., 1999, J. Appl. Phys., 85, 6711
- Trolier-McKinstry, S., 2011, private communication
- Schwartz, D. A. et al., 2011 (SPIE), vol. 8147
- Heilmann, R. K. et al., 2010, in M. Arnaud, S. S. Murray & T. Takahashi, eds., in *Space Telescopes and Instrumentation 2010: Ultraviolet to Gamma Ray*, vol. 7732, 77321J
- Falcone, A. D. et al., 2007, in *Society of Photo-Optical Instrumentation Engineers (SPIE) Conference Series, Society of Photo-Optical Instrumentation Engineers (SPIE) Conference Series*, vol. 6686
- Suntharalingam, V. et al., 2007, in *Society of Photo-Optical Instrumentation Engineers (SPIE) Conference Series, Society of Photo-Optical Instrumentation Engineers (SPIE) Conference Series*, vol. 6690
- Janesick, J. et al., 2007, in *Society of Photo-Optical Instrumentation Engineers (SPIE) Conference Series, Society of Photo-Optical Instrumentation Engineers (SPIE) Conference Series*, vol. 6690
- Lechner, P. et al., 2010, in *Society of Photo-Optical Instrumentation Engineers (SPIE) Conference Series, Society of Photo-Optical Instrumentation Engineers (SPIE) Conference Series*, vol. 7742
- Smith, S.J. et al., 2009, IEEE Transactions on Applied Superconductivity, 19, no. 3, 451
- Smith, S.J. et al., 2008, Proc. SPIE, 7011, 701126
- Irwin, K.D. et al., 2011, arXiv:1110.1608
- Brenneman, L. et al., 2009, in *astro2010: The Astronomy and Astrophysics Decadal Survey*, *Astronomy*, vol. 2010, 26–+
- Springel, V. et al., 2005, *Nature*, 435, 629, millenium simulation
- Vikhlinin, A. et al., 2009, in *astro2010: The Astronomy and Astrophysics Decadal Survey*, *Astronomy*, vol. 2010, 304–+
- Fan, X. et al., 2006, *The Astronomical Journal*, 132, no. 1, 117
- Willott, C. J. et al., 2010, *The Astronomical Journal*, 140, no. 2, 546
- Mortlock, D. J. et al., 2011, *Nature*, 474, 616
- Volonteri, M., 2010, *A&A Rev.*, 18, 279
- Shemmer, O. et al., 2006, *The Astrophysical Journal*, 644, no. 1, 86

24. Anderson, M. E. & Bregman, J. N., 2011, *The Astrophysical Journal*, 737, no. 1, 22
25. Kereš, D. et al., 2009, *Monthly Notices of the Royal Astronomical Society*, 395, no. 1, 160
26. Chartas, G. et al., 2009, *ApJ*, 706, 644
27. Li, Y. et al., 2007, *ApJ*, 665, 187
28. Merloni, A. & Heinz, S., 2008, *MNRAS*, 388, 1011
29. Leauthaud, A. et al., 2011, *ArXiv e-prints*
30. McGaugh, S. S. et al., 2010, *The Astrophysical Journal Letters*, 708, no. 1, L14
31. Croton, D. J. et al., 2006, *Monthly Notices of the Royal Astronomical Society*, 365, 11
32. Governato, F. et al., 2010, *Nature*, 463, 203
33. Matsuda, Y. et al., 2011, *Monthly Notices of the Royal Astronomical Society: Letters*, 410, no. 1, L13
34. Broos, P. S. et al., 2011, *ApJS*, 194, 2
35. Brickhouse, N. S. et al., 2010, *ApJ*, 710, 1835
36. Kaastra, J. S. et al., 2000, *Astronomy and Astrophysics*, 354, L83
37. Wong, K.-W. et al., 2011, *The Astrophysical Journal Letters*, 736, no. 1, L23
38. Steidel, C. C. et al., 2010, *The Astrophysical Journal*, 717, no. 1, 289
39. Erb, D. K. et al., 2006, *The Astrophysical Journal*, 647, no. 1, 128
40. Feigelson, E. D., 2010, *Proceedings of the National Academy of Science*, 107, 7153
41. Kaspi, S. et al., 2002, *The Astrophysical Journal*, 574, no. 2, 643
42. Paerels, F. et al., 2009, in *astro2010: The Astronomy and Astrophysics Decadal Survey*, *Astronomy*, vol. 2010, 230–+
43. Markevitch, M. et al., 2003, *The Astrophysical Journal*, 583, no. 1, 70